TU Delft

Delft University of Technology

Intergranular corrosion of TiNb-microalloyed martensitic stainless steels processed by quenching and partitioning

Li, Gaojie; Santofimia Navarro, Maria J.; Gonzalez-Garcia, Yaiza

DOI
10.1016/j.jmrt.2025.08.255

Licence
CC BY

Publication date
2025

Document Version
Final published version

Published in
Journal of Materials Research and Technology

Citation (APA)
Li, G., Santofimia Navarro, M. J., & Gonzalez-Garcia, Y. (2025). Intergranular corrosion of TiNb-microalloyed martensitic stainless steels processed by quenching and partitioning. *Journal of Materials Research and Technology*, *38*, 4713-4722. https://doi.org/10.1016/j.jmrt.2025.08.255

Important note
To cite this publication, please use the final published version (if applicable).
Please check the document version above.

Copyright
Other than for strictly personal use, it is not permitted to download, forward or distribute the text or part of it, without the consent of the author(s) and/or copyright holder(s), unless the work is under an open content license such as Creative Commons.

Takedown policy
Please contact us and provide details if you believe this document breaches copyrights.
We will remove access to the work immediately and investigate your claim.

This work is downloaded from Delft University of Technology.
For technical reasons the number of authors shown on this cover page is limited to a maximum of 10.

Journal of Materials Research and Technology 38 (2025) 4713–4722

Contents lists available at ScienceDirect

Journal of Materials Research and Technology

journal homepage: www.elsevier.com/locate/jmrt

Intergranular corrosion of TiNb-microalloyed martensitic stainless steels processed by quenching and partitioning

Gaojie Li, Maria J. Santofimia Navarro, Yaiza Gonzalez-Garcia *

Department of Materials Science and Engineering, Delft University of Technology, Mekelweg 2, Delft, 2628 CD, the Netherlands

ARTICLE INFO

Keywords:
Martensitic stainless steel
Q&P
Intergranular corrosion
Ti
Nb microalloying
TEM
SKPFM

ABSTRACT

This study investigates the localised corrosion mechanisms in laboratory-processed Q&P-treated martensitic stainless steels. Two steel variants, one NbTi-free (alloy B) and the other micro-alloyed with Nb and Ti (alloy M) were investigated to elucidate the influence of microalloying on corrosion behaviour.

Both NbTi-free and NbTi-micro alloyed martensitic stainless steels were examined using a combination of electrochemical methods (potentiodynamic polarisation and double-loop electrochemical potentiokinetic reactivation) and microstructural analysis (Transmission Electron Microscopy and scanning Kelvin probe force microscopy). Potentiodynamic polarisation results showed no significant differences between the alloys and no clear evidence of pitting corrosion. Optical analysis of the specimens showed preferential attack at grain boundaries. Double-loop electrochemical potentiokinetic reactivation measurements revealed a higher degree of sensitisation to intergranular corrosion in the microalloyed steel compared to the NbTi-free variant. Transmission Electron Microscopy showed that intergranular corrosion in both steels originated from chromium depletion zones adjacent to chromium carbides along grain boundaries. The increased susceptibility in the microalloyed steel was linked to the presence of TiN(Nb) particles. Scanning Kelvin probe force microscopy further revealed variations in surface potential at grain boundary precipitates and depleted zones, emphasising their role in intergranular corrosion initiation.

These findings emphasise the critical influence of processing routes on the corrosion mechanisms of Q&P-treated martensitic stainless steel.

1. Introduction

Driven by increasing demands for lighter vehicles and the global push to reduce carbon emissions—of which the steel industry is responsible for approximately 20 % within the manufacturing sector—optimizing existing steel grades presents a cost-effective and practical alternative to developing entirely new materials. Through the adjustment of manufacturing parameters and heat treatments, it is possible to enhance the performance of existing steels while simultaneously reducing energy consumption and emissions [1–7]. In this context, the third generation of advanced high-strength steels (AHSS) has seen considerable development in recent decades. Among these, AHSS produced via quenching and partitioning (Q&P) processing has received growing attention due to its excellent combination of high strength and ductility [5–7].

Beyond carbon steels, Q&P treatment also shows potential for application in martensitic stainless steels, resulting in a microstructure consisting of carbon-enriched austenite and carbon-depleted martensite [8–13]. However, most existing studies have concentrated on microstructure evolution, phase fraction, and mechanical property evaluation [8–12]. To date, only one study has investigated the local corrosion resistance of Q&P-treated stainless steels, reporting that this property can be improved compared to conventional quenching and tempering treatments [13]. Nevertheless, the relationship between corrosion behavior and the resulting microstructure remains largely unexplored. Understanding the corrosion behavior of Q&P-treated martensitic stainless steels will help guide their application in corrosion-sensitive environments and support the development of new heat treatment strategies tailored for enhanced performance.

In stainless steels, intergranular corrosion (IGC) is reported to be one of the primary corrosion mechanisms [14–22]. IGC occurs due to an electrochemical potential difference between the matrix and chromium-depleted regions, which form as a result of Cr-carbide precipitation along grain boundaries. Microalloying with elements such as

* Corresponding author.
E-mail address: y.gonzalezgarcia@tudelft.nl (Y. Gonzalez-Garcia).

https://doi.org/10.1016/j.jmrt.2025.08.255
Received 15 April 2025; Received in revised form 18 August 2025; Accepted 27 August 2025
Available online 28 August 2025
2238-7854/© 2025 The Authors. Published by Elsevier B.V. This is an open access article under the CC BY license (http://creativecommons.org/licenses/by/4.0/).

Nb and Ti has been shown to effectively reduce the risk of IGC, as these elements preferentially form stable carbides and nitrides, thereby suppressing the formation of Cr-carbides [14–22]. However, the influence of alloy design and the specific role of microalloying elements like Nb and Ti in Q&P-treated stainless steels has not yet been systematically investigated. In particular, the impact of Nb and Ti on the IGC behavior of martensitic stainless steels remains largely unexplored.

In our previous research, a new class of martensitic stainless steels was designed through the accurate selection of chemistries and heat treatment parameters [12,23,24]. We found that chromium carbides precipitate at the grain boundaries before the partitioning treatment in these newly designed martensitic stainless steels [24]. However, the corrosion behavior at grain boundaries cannot be clearly observed. We found that the corrosion resistance of Q&P steels is primarily controlled by the presence of MnS and TiN inclusions, with chemical composition and phase fractions playing a less significant role. This phenomenon is evident in industrially produced materials, where MnS inclusions are formed. The addition of microalloying elements Ti and Nb leads to the formation of particles such as NbC and TiN, which contribute to the refinement of prior austenite grain size, as demonstrated and quantified in our previous work [12,23]. However, when these particles precipitate and grow to micrometer size, they can also promote the formation of new inclusions that may facilitate the initiation of localized corrosion [23].

This work investigates the role of microalloying elements on the corrosion behaviour of Q&P-processed martensitic stainless steels under lab conditions. Q&P treated 0.3 wt% C – 13 wt% Cr martensitic stainless steels are investigated without and with 0.05 wt% Ti and 0.05 wt% Nb. Microstructure and grain boundaries are characterised using scanning electron microscopy (SEM), transmission electron microscopy (TEM) equipped with energy dispersive spectroscopy (EDS), and scanning Kelvin probe force microscopy (SKPFM). Potentiodynamic polarisation (PDP) and double-loop electrochemical potentiokinetic reactivation (DL-EPR) tests are conducted to inspect the susceptibility of the samples to localised corrosion and to IGC sensitisation, respectively.

2. Experimental procedure

2.1. Materials and heat-treatment

The chemical compositions of the two stainless steels investigated in this work are given in Table 1. The NbTi-free steel is denoted as the base steel (abbreviated as "B"), while the NbTi-microalloyed steel is referred to as the microalloyed steel (abbreviated as "M"). Steel ingots were cast by Acerinox (Spain) and further processed in RINA-CSM (Italy). After homogenization at 1270 °C for 3 h, the material was hot-rolled with the last pass at 1000 °C and cooled down to room temperature at a rate of 0.1 °C/s, leading to 100 × 20 × 2 cm^3 slabs. Subsequently, an annealing treatment was performed at 600 °C for 24 h to soften the material.

Cylindrical specimens 10 mm in length and 4 mm in diameter were machined by electron discharge machining from the slabs with the long axis parallel to the rolling direction. Heat treatments were applied with a DIL805 D Bähr/TA dilatometer to obtain different Q&P microstructures. The temperature was controlled using an S-type thermocouple that is spot-welded onto the middle of the cylindrical specimens. Two quartz rods were used for clamping and flexible fixing specimens. During the heating and isothermal holding segments, a vacuum of approximately 10^{-4} mbar was maintained in the chamber. Helium was used as a cooling mediate. Fig. 1 shows a scheme of the heat treatments applied to the cylindrical specimens in the dilatometer. The heat treatment parameters were selected in our previous work [24].

Table 1
Chemical composition of the studied martensitic stainless steel (wt.%).

Alloy	Fe	C	Mn	Si	Cr	Ni	Al	N	Nb Ti
B	Bal.	0.30	3.0	0.35	13	0.2	0.01	0.03	–
M	Bal.	0.30	3.0	0.35	13	0.2	0.01	0.03	0.05-0.05

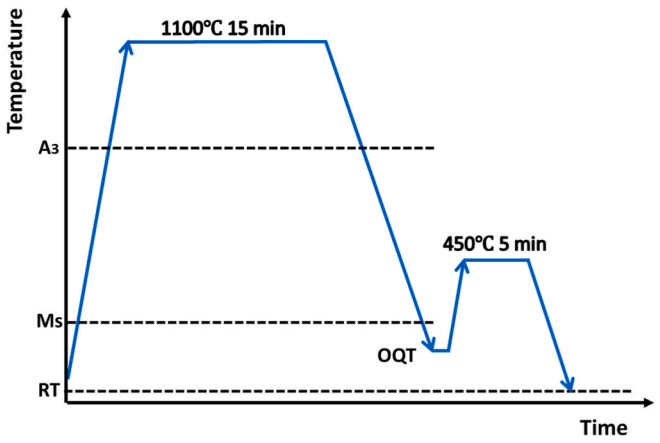

Fig. 1. Applied Q&P heat treatment on samples. The optimum quench temperature (OQT) was 50 °C and 62 °C for sample B and sample M, respectively.

The Q&P specimens were first austenitized at 1100 °C for 15 min to obtain full austenitic microstructure, followed by cooling to the optimum quench temperature (OQT) [5], 50 °C and 62 °C, corresponding to sample B and M, respectively. Then, the quenched specimens were reheated at 450 °C and held at this temperature for 5 min to allow the partitioning of carbon from martensite to austenite. The process ended with quenching again to room temperature.

2.2. Microstructural characterisation

After heat treatment, the cylindrical specimen was cross-sectionally cut perpendicular to its axis, and the exposed cross-section was then ground and polished for subsequent testing. The surface of the samples was prepared using standard metallographic procedures and finished with OPS (Oxide Polishing Suspensions) polishing for 15 min. A Vilella reagent (ASTM E407-80) consisting of 1 g picric acid, 5 ml HCl and 100 ml ethanol was employed. Optical microscopy (Digital Keyence VHX-5000 and optical LEICA DMLM) and a Field Emission Gun Scanning Electron Microscope (FEG-SEM, JEOL JSM-6500F) operating at 15 kV and 10 mm working distance were used to characterise the microstructure.

Thin cross-sections of the samples were made with a TFS Helios Nanolab G3 and secured on the copper half grids for TEM examinations using the lift-out procedure. A 200-nm-thick layer of Pt was deposited initially with a 2-keV electron beam, followed by ion-beam deposition until reaching a Pt thickness of approximately 1 μm. The thinning-down process was done with the Ga ion beam at 30 keV, followed by a quick cleaning at 5 keV.

TEM investigations were performed with a TFS Talos F200X equipped with 4 in-column SDD Super-X detectors. Bright-field (BF) and dark-field (DF) TEM images were taken by inserting objective aperture and beam tilt to choose desired diffraction spots. High-angle annular dark field (HAADF)-STEM/EDS were carried out to elementally map the samples, revealing different particles.

The phase fraction after Q&P heat treatment is the same for both alloys, with austenite 57 % and martensite 43 %, confirmed by XRD measurement.

2.3. Electrochemical tests

The heat-treated cylindrical specimens, after being cross-sectionally cut, were embedded in epoxy resin with only their central circular cross-section exposed. The exposed surface was then prepared using standard metallographic procedures, including grinding and polishing, to achieve

a high-quality testing surface. Conventional electrochemical experiments using potentiodynamic polarisation (PDP) are performed using a Biologic VSP-300 potentiostat supported by EC-Lab V11.36 software. The experimental setup was a three-electrode cell, using an Ag/AgCl/KCl (sat.) electrode as a reference electrode (RE), a platinum mesh as a counter electrode (CE), and the sample as the working electrode (WE). The potential scan rate was 0.167 mV/s from −200 mV vs. OCP until the breakdown potential. Prior to PDP measurement, the open circuit potential (OCP) was measured for 1.5 h, at which steady-state is achieved. Aerated 3.5 wt% NaCl aqueous solution was used as the electrolyte, and measurements were carried out at room temperature (~20 °C). At least four repetitions were carried out to confirm the reproducibility of the experiments.

The specimens were evaluated for degree of sensitisation (DOS) using a double loop electrochemical potentiokinetic reactivation (DL-EPR) test in 0.01 M H_2SO_4 solution at room temperature. The potential scan rate was 1.66 mV/s from −600 mV to +200 mV vs. the reference electrode and then immediately reversed to the starting point as the same scanning rate. The DL-EPR test conditions were selected and optimized based on various parameters, including depassivator type, electrolyte composition, potential window, and scan rate, as referenced in Refs. [25,26]. These conditions were chosen to produce clearly distinguishable peaks, enabling correlation with the observed microstructural morphology under microscopy. DOS was reported as the ratio of maximum current density in the reactivation loop (I_r) to the curren t density in the activation loop (I_a). At least five repetitions were carried out to confirm the reproducibility of the experiments, and the average values were reported.

The SKPFM measurements were performed in the tapping mode using a Bruker Dimension EdgeTM instrument with Nanodrive v8.05 software. A rectangular conductive cantilever (silicon pyramid single-crystal tip coated with PtIr5, SCM-Pit probe) was employed. A direct current (DC) bias potential was applied to the AFM tip for all measurements. All AFM/SKPFM measurements were performed with a scan rate of 0.15 Hz and a pixel resolution of 512 × 512. The raw data was analysed using Gwyddion 2.60 software. The KPFM measures contact potential difference (CPD) between a conducting AFM tip and a sample. The CPD (V_{CPD}) between the tip and sample is defined as:

$$V_{CPD} = \frac{\Phi_{tip} - \Phi_{sample}}{-e}$$

Where Φ_{sample} and Φ_{tip} are the work functions of the sample and tip, and e is the electronic charge. When an AFM tip is brought close to the sample surface, an electrical force is generated between the tip and sample surface, due to the differences in their Fermi energy levels [27]. The amount of applied external bias that nullifies the electrical force due to the V_{CPD} is equal to the work function difference between the tip and sample; therefore, the work function of the sample can be calculated when the tip work function is known.

3. Results

3.1. OM and SEM microstructures

Fig. 2 illustrates the OM and SEM micrographs of the microstructures of the two Q&P treated alloys. OM images in Fig. 2 (a) and (b) show that the prior austenite grains were mostly equiaxial. It is also evident that the prior austenite grain size (PAGS) of alloy B is much larger than that of alloy M. The quantitative PAGS statistics indicate that the average PAGS of alloy B is 103 ± 43 μm and of alloy M is 30 ± 15 μm. On the sample surface of alloy M, bright yellow particles were observed, which have been confirmed as TiN particles in Ref. [23].

Furthermore, segregation bandings are also observed in both samples. From Refs. [24,28], the dark etched bands correspond to martensite-rich bands and the bright bands to austenite-rich. The selective etching of bands is caused by the elemental segregation of Cr and Mn content during the Q&P treatment. The higher resolution SEM images in Fig. 2 (c) and (d) illustrate that, in both alloys, there is carbide precipitation at the grain boundaries. As reported in our previous work [24], the carbides at grain boundaries precipitated before partitioning and remained in the final microstructure. Furthermore, Fig. 2 (d) shows a large TiN particle. TiN particles are primarily distributed at or adjacent to the prior austenite grain boundaries.

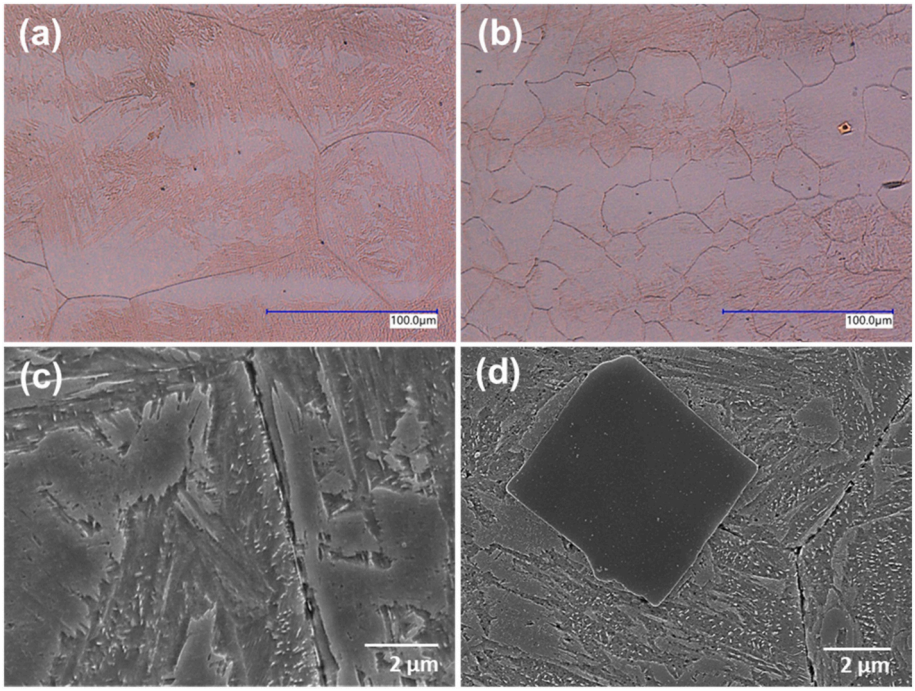

Fig. 2. OM and SEM microstructures of Q&P treated alloys after etching for 15 s: (a)(c) alloy B, and (b)(d) alloy M.

3.2. Electrochemical characterisation

The corrosion properties of the samples were studied using PDP experiments to investigate the effect of microstructural characteristics on corrosion performance. Fig. 3 (a)(b) show representative curves and corresponding analysis. Fig. 3 (c)(d) display OM images of the specimens after the potentiodynamic polarisation tests.

The curves in both samples (Fig. 3 (a)) showed very similar passivity ranges but did not show a sharp breakdown potential. Instead, there is a gradual increase of current density until a more dramatic change at around a potential of 0 V when we can consider a failure of the passivity. Fig. 3 (b) compares the corrosion current density (i_{corr}) and corrosion potential (E_{corr}) extrapolated from PDP curves, respectively. The corrosion current density and potential values for both alloys fall relatively into the same range.

No signs of pitting corrosion were observed in either alloy based on the potentiodynamic polarisation curves. After the applied potential exceeded the upper limit of the test window, the sample surfaces were examined using optical microscopy to assess the corrosion patterns at higher potentials. The optical images taken after testing (Fig. 3(c)(d)) showed no evidence of pits on the surface of the samples. Instead, the prior austenite grain boundaries appear preferentially attacked for both alloys. Especially in alloy M, the grain boundaries (GBs) are severely corroded, leading to areas with prior austenite grain dropout, which is consistent with the grain dropout phenomenon previously documented in the literature [14,17,18]. The preferential attack of grain boundaries and absence of pits could explain the absence of a sharp breakdown potential in the PDP curves.

To further confirm and quantify the susceptibility to intergranular corrosion, DL-EPR experiments are carried out, and the degree of sensitisation (DOS) is estimated for both Q&P-treated samples. Fig. 4 shows DL-EPR results for the Q&P treated specimens. From Fig. 4 (a), typical DL-EPR curves are seen with significant activation current peaks (I_a) and small reactivation current peaks (I_{r1} and I_r). During the anodic scan, the entire surface is activated to form the activation current peak at a potential of approximately −0.35 V (E_a). Then, the current decreased within a wide passivity range from −0.35 V to 0.2 V, in which a wide passive film can form on the surface. There is no significant difference between samples regarding the activation scan.

In the reverse scan, the reactivation current peaks are attributed to the defects of passive films, such as the Cr-depleted zones. There is more than one reactivation current peak in each alloy, referred as I_{r1} and I_r peaks. The presence of two reactivation peaks can be attributed to not homogenous sensitisation of the steels with not only the Cr-depleted zones but also other features in the microstructure. As observed in the microstructure anlaysis and discussed in our previous research [24,28], these Q&P treated samples present chemical segregation bands. This could explain the appearance of a second reactivation peak. The second reactivation peak at a lower potential value is the one attributed to the IGC [29]. These peaks for the investigated alloys are approximately at a potential (E_r) value of −0.4 V. The DOS to IGC of each specimen is measured by the ratio I_r/I_a, corresponding to the reactivation (I_r) and activation (I_a) current peaks identified in the curve. The DOS values estimated from the curves are shown in Fig. 4 (b). The average DOS value for alloy B is 0.73 ± 1.07 %, which indicates very low susceptibility to IGC, while alloy M showed a higher value, 3.75 ± 1.13 %, considered in the range of moderate susceptibility.

3.3. Grain boundary analysis

TEM and STEM measurements are employed to characterise the grain boundaries at the nanoscale. Fig. 5 shows the FIB cutting location, TEM micrographs, and EDS analysis results for both alloys. For the case of alloy B, Fig. 5 (a)(b) shows the cutting location at the grain boundary

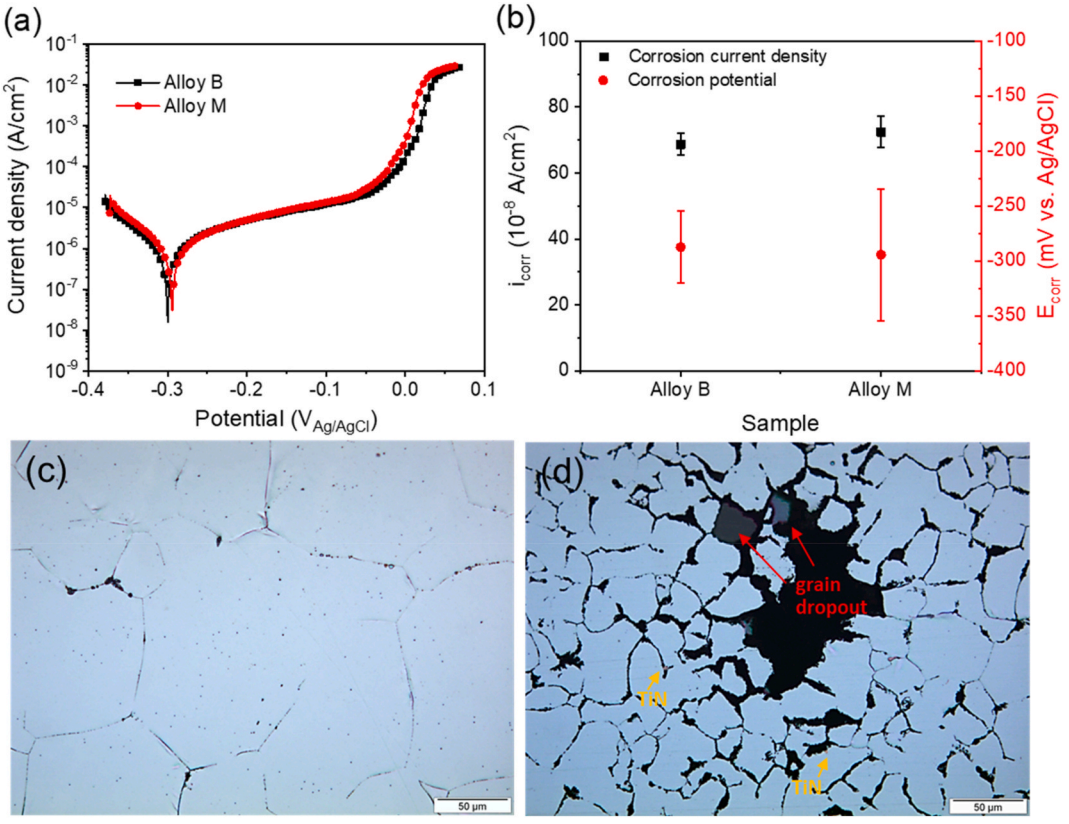

Fig. 3. (a) Selected potentiodynamic polarisation curves and (b) averaged values of the corrosion potential of alloys B and M. (c)(d) OM microstructures after polarisation of alloy B alloy M, respectively.

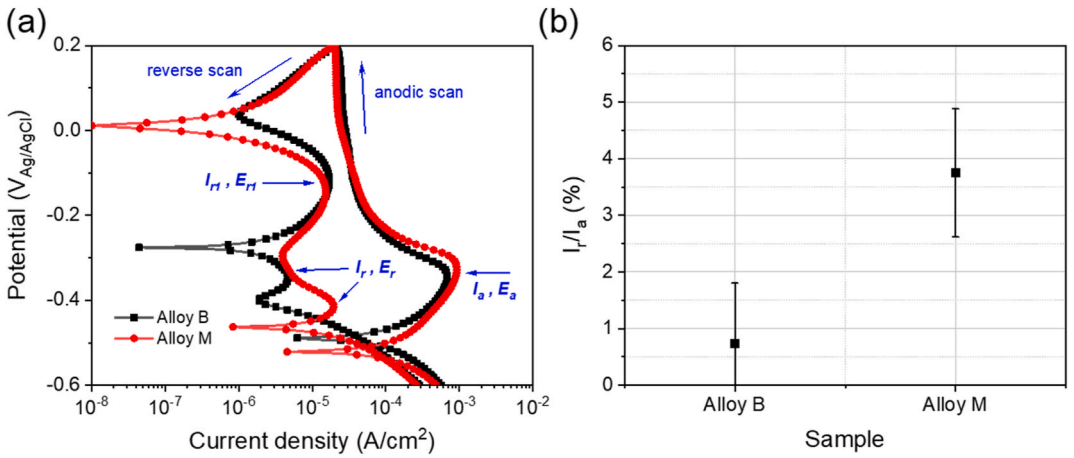

Fig. 4. (a) DL-EPR curves plotted for alloys B and M after Q&P heat treatment, (b) corresponding degree of sensitisation (DOS) values. The values and scatter bars are obtained from an average of five experiment repetitions.

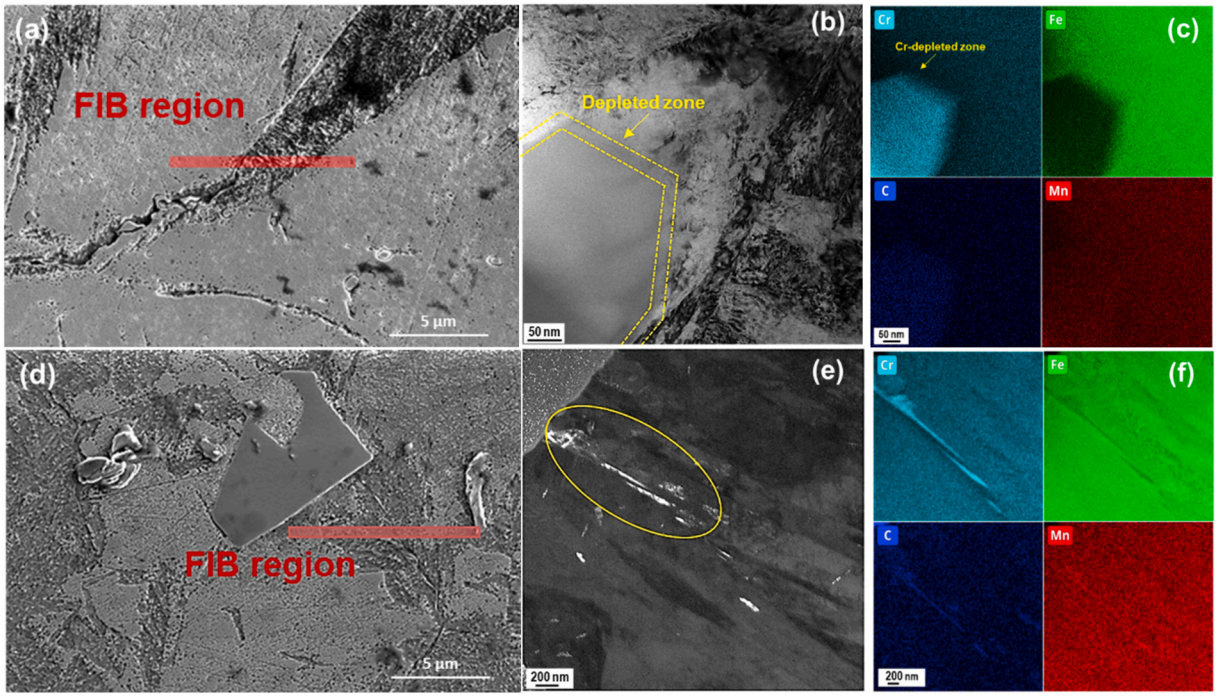

Fig. 5. FIB cutting region, TEM microstructure of GB precipitate, and elemental analysis of GB precipitate in alloys B (a)(b)(c) and M (d)(e)(f), respectively.

containing a carbide particle with a diameter of approximately 200 nm. The EDS analysis indicates that this particle is Cr-carbide, and a Cr-depleted zone in the vicinity of the particle is observed, as pointed out in the figure. For alloy M, as shown in Fig. 5 (d), a FIB cut is also made from a grain boundary location, specifically near a TiN particle with a size of 5 μm. The particle with a length of 200 nm is observed in Fig. 5 (e). The EDS analysis of the precipitate also shows high chromium and carbon contents. As such, in both alloys, these GBs precipitation are Cr-carbides.

Fig. 6 displays the STEM with EDS mapping of one representative particle in alloy M. The spherical particles with a diameter of approximately 50 nm were widely observed at (grain and phase) interfaces. EDS analysis shows high contents of Ti, Nb and N, low content of Cr and Fe. The Ti and N atoms are primarily located in the particles' centre and surrounded by Nb. These nano-size TiN(Nb) particles have the same/similar composition as the big rectangular/triangle bright yellow particles (in Fig. 2). Note: TiN constitutes the main body of the particle, while the detection of Nb may vary depending on testing factors such as resolution or operational parameters. Therefore, these Ti- and/or Nb-containing microalloyed particles are generally referred to as TiN(Nb).

Ti- and Nb-containing microalloyed particles of varying sizes are widely studied in HSLA steels for precipitation-strengthening purposes [30–33]. It is reported that heterogeneous nucleation sites such as grain boundaries, dislocations, or second-phase particles are preferable for insoluble TiN particles [30]. The formation of such complex precipitates follows a sequential process, in which Ti-based nitrides or carbides form first, followed by the precipitation of Nb. The Nb-rich particles subsequently nucleate on the habit planes of the pre-existing Ti-containing phases, resulting in the formation of a so-called "core–shell" structure [31]. TEM analysis demonstrates that the GBs of alloy M contain not only Cr-carbides but also TiN(Nb) macroparticles (10 μm) and nanoparticles (50 nm).

In order to further verify the possible different reactivity of the grain boundaries due to the presence of the different precipitates, surface

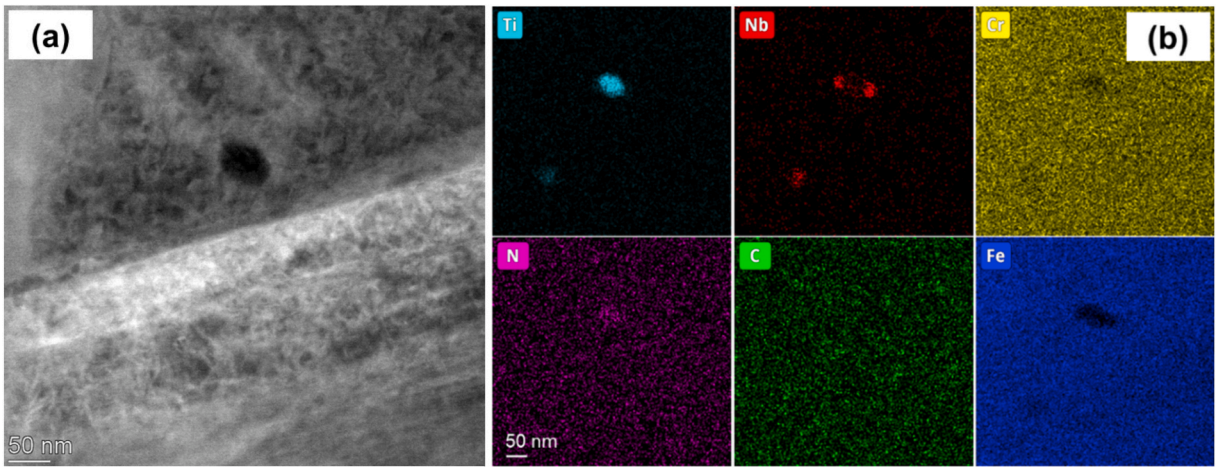

Fig. 6. (a) TEM microstructure and (b) elemental analysis of precipitate particle in alloy M.

Volta potential mapping by SKPFM is performed along the grain boundaries of the investigated steels.

Fig. 7 displays the SKPFM topography and Volta potential maps, and the corresponding SEM micrographs. To localise the grain boundaries during SKPFM experiments, the samples were slightly etched using a Vilella reagent solution. Topography maps of both samples in Fig. 7 (a) and (e) show that the GBs appear as trenches across the matrix. For alloy B, the Volta potential map in Fig. 7 (b) shows that the GBs are brighter and have a higher Volta potential than the surrounding matrix. Fig. 7 (c) shows an enlarged GB region from which the liner Volta potential profile was made. Lines 1–3 are made over grain boundaries with Cr-carbides, while Line 0 is over grain boundaries without carbide precipitation. The corresponding Volta potential distribution in Fig. 7(d) shows some difference between the matrix and the GBs. For Line 0, the surface potential waved within the 4 mV range, and there are no potential peak links to carbide. The peaks of the Volta potential at Lines 1–3 are linked to the Cr-carbides precipitated inside GBs. The drop of the Volta potential originates from the Cr-depleted zone induced by Cr-carbide precipitation, as previously displayed in Fig. 3. The Volta potential difference between the Cr-carbide and Cr-depleted zone is up to 9.8 mV, as the graph indicates.

For the case of alloy M, as seen in Fig. 7(e–h), the GBs on the sample surface exhibit the same characteristics as that of alloy B. The Cr-depletion occurring adjacent to the Cr-carbide precipitation leads to low Volta potential, as well the Volta potential peak was recorded on the Cr-carbides, and the potential difference reaches approximately 9.2 mV. For the line profile over the grain boundary without carbide precipitation, Line 0 shows no signs of a potential peak. Apparently, the Volta potential difference will contribute to the susceptibility to IGC of the investigated Q&P steels, and the Cr-depleted zone in the vicinity of Cr-carbides would be the active dissolution region when exposed to a corrosive environment.

OM and SEM revealed the presence of micron-sized particles, while TEM identified nanoscale particles. Since grain refinement is primarily driven by the pinning effect of microalloying particles, it is likely that more nanoscale particles are present at grain boundaries than can be directly observed. These particles may influence grain boundary activity. Therefore, a readily identifiable micron-sized particle was selected for detailed characterization to represent the properties and role of microalloying particles. The interplay of these factors on susceptibility to IGC requires further clarification. To explore this further, in alloy M, the Volta potential distribution along the TiN(Nb) particles was measured using SKPFM. The topography, Volta potential maps and liner Volta potential profiles are shown in Fig. 8 below. As can be seen from Fig. 8 (a), the TiN(Nb) particle stands out from the matrix and has a much higher Volta potential value than the matrix. As already reported in Refs. [23,34]. The liner profiles cross the particle in Fig. 8 (c) show that the Volta potential of the TiN(Nb) particle is 100 mV higher than that of the matrix. The difference in the chemical composition of TiN (Nb) may affect the Volta potential. Thus, line 2 differs from line 1 regarding the Volta potential measured on the TiN(Nb).

The interface between particle and matrix on both line profiles, as indicated in the figure, shows a significant Volta potential drop of 10 mV compared to the matrix. This can be attributed to the difference in chemical composition at the interface, i.e. the Nb clustering, as observed under TEM in Fig. 6.

As such, the phase exhibiting positive Volta potentials relative to the matrix would show cathodic behaviour [29]. The dissolution currents and in-situ corrosion behavior have been documented in our previous work [23], where the current signal at the particle–matrix interface was captured in situ in the electrolyte, and a corrosion trench was observed after the electrochemical test. Thus, the TiN(Nb) particle with a relatively high Volta potential would serve as the micro-cathode, and the surrounding steel matrix (specifically, the interface) would serve as the micro-anode. Considering that the TiN(Nb) particles were also identified at GBs in the case of alloy M, they can exacerbate the sensitivity of IGC, which was initially only caused by Cr-carbides. As a result, its DOS to IGC is higher than alloy B, as reported in Fig. 4.

4. Discussion

The Q&P martensitic stainless steels processed under laboratory conditions in this work exhibited a different corrosion mechanism from the previously reported pitting corrosion [23]. Cr-carbides are present in both alloys, even after the Q&P heat treatment. The microalloying elements Nb and Ti did not play a role in reducing the precipitation of Cr-carbides at grain boundaries, as reported previously for the case of ferritic stainless steels [14–22]. Contrary to our previous work [23], in this case, pitting corrosion is not the dominant mechanism, given the absence of inclusions. In this case, the grain boundaries of the martensitic steels became the preferential sites for localised attack.

The addition of microalloying elements Nb and Ti refined the prior austenite grain size from 103 ± 43 μm in alloy B to 30 ± 15 μm in alloy M. TiN(Nb) precipitation was observed in alloy M. However, the electrochemical results revealed no significant difference in the corrosion resistance when considering the differences in the chemical composition of the alloys and different grain sizes. The influence of grain size on the corrosion resistance of different stainless steels has been reviewed by Ralston et al. [35]. Refining of the grain size is reported to increase or decrease the susceptibility to corrosion depending on the alloy and the processing route. In the case of alloy B and alloy M, these were not observed. Potentiodynamic polarisation results showed no significant

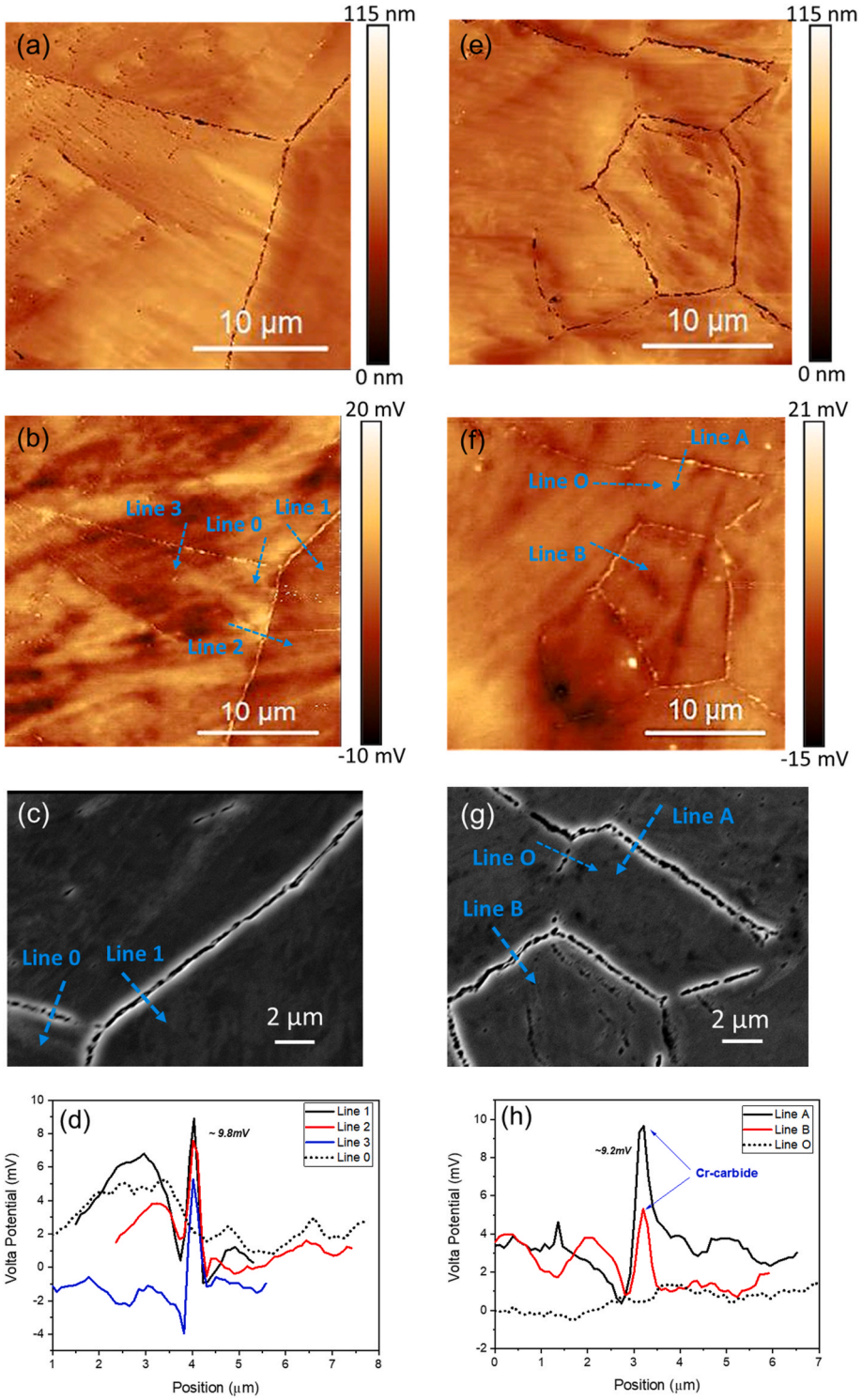

Fig. 7. The topography, Volta potential maps, SEM micrograph, and liner Volta potential profiles across the grain boundaries, respectively, of alloy B (a–d) and alloy M (e–h) on the etched sample surface.

differences between the alloys.

The presence of Cr-carbides at grain boundaries, confirmed by TEM analysis, explains the susceptibility of the alloys to intergranular corrosion. The degree of susceptibility (DOS) increases in alloy M due to the additional presence of TiN(Nb) particles. TEM and SKPFM results demonstrated that, in both alloys, the Cr-depleted regions (Cr-carbide/matrix interface) were preferentially dissolved as the anode during the corrosion process, while the Cr-(rich)carbide in GBs was not dissolved as the cathode. Additionally, in alloy M, TiN(Nb) particle was detected both in the macro scale (10 μm under SEM) and nanoscale (50 nm under TEM). An extra galvanic effect was thereby formed, in which the TiN (Nb)/matrix interface (probably Nb clustering) served as the anode during the corrosion process, while the TiN(Nb) particle was the cathode.

From these results, the IGC mechanism is elucidated in the diagram of Fig. 9. For the case of alloy B, the IGC process can be seen in Fig. 9

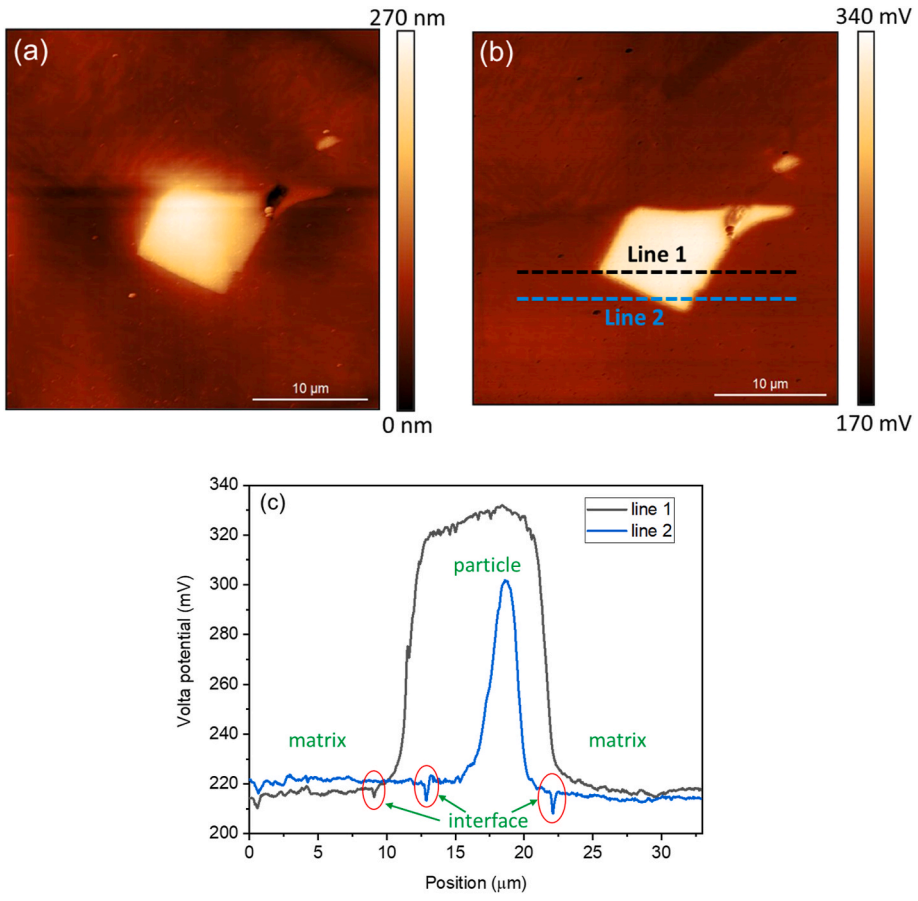

Fig. 8. (a)Volta-potential map, (b)topography map, and (c) line profile of TiNb particle in alloy M (polished surface).

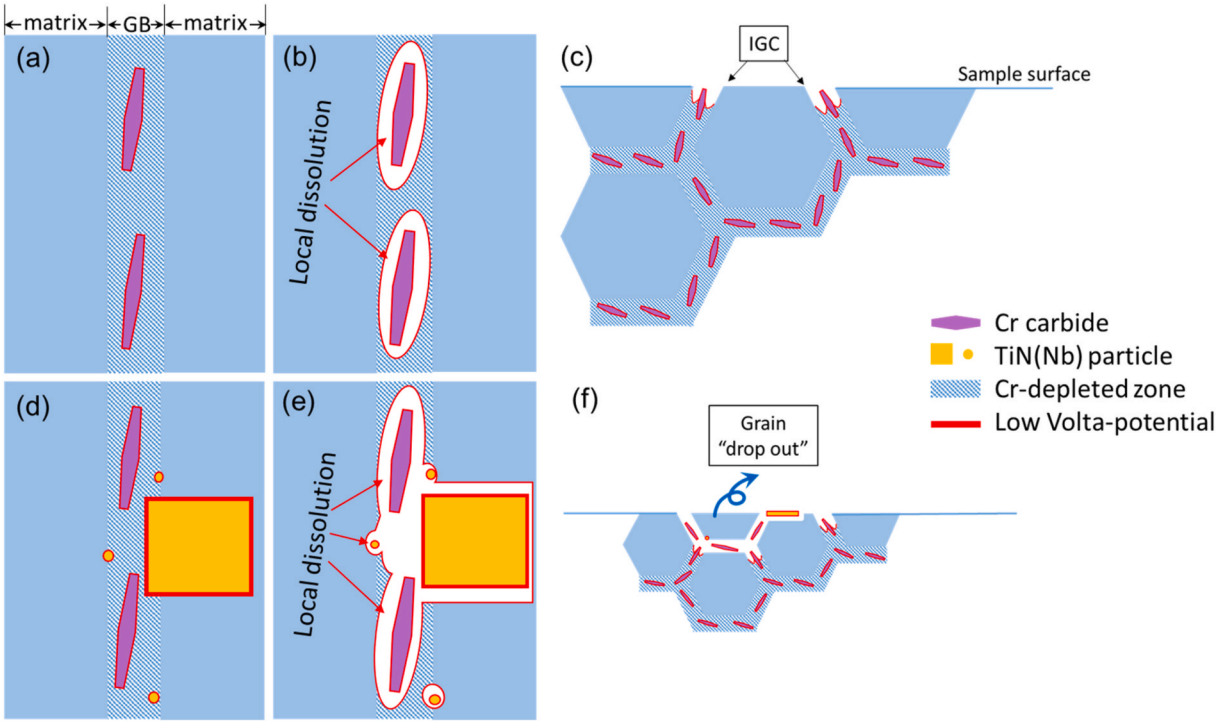

Fig. 9. Schematic diagram illustrating the grain boundary microstructure, local dissolution of grain boundary in electrolyte and cross-section view in an electrolyte, respectively, of alloy B (a–c) and alloy M (d–f).

(a–c). The grain boundaries (GBs) region contains Cr-carbides and adjacent Cr-depleted zone. The interface of the Cr-carbides, indicated in red, shows a lower Volta potential. When the sample surface is exposed to corrosive environments, such as NaCl solution (illustrated in Fig. 9 (b)), the presence of chloride ions (Cl^-) makes the GBs and the particle/matrix interfaces particularly susceptible to anodic dissolution. Starting from a selected dissolution of the matrix around particles at GBs, the dissolution process gradually extends into the Cr-depleted zone over time. Eventually, the isolated localised corrosion sites deepen and merge, resulting in the formation of corrosion ditches along the GBs, which is characteristic of intergranular corrosion.

For the case of alloy M, as shown in Fig. 9(d–f), not only the Cr-carbides interface but also the TiN(Nb) particle interface becomes the anodic sites. It would continuously exert the galvanic effect during the whole localised corrosion process. Thus, it will take a shorter time for separated local corroding sites at the boundary to connect, leading to intergranular corrosion. For specific locations with macro-size TiN(Nb) particles, the micro-galvanic effect is still triggered, enhancing the attack of the surrounding matrix and generating deeper trenches and with the possible neighbouring grain "dropout", as reported in Refs. [14,17,18]. This leads to extensive localised corrosion attack observed in Figs. 3 and 9 (f). In summary, the presence of Cr-carbides at GB compromises the corrosion resistance of the steel, leading to IGC as a failure mechanism. The addition of micro-alloying elements increases the susceptibility of the steel to IGC on these samples due to the formation of nano- and micro-meter TiNb precipitates also located at the grain boundaries and surroundings, respectively.

Based on the present findings and previous studies, two potential strategies can be proposed to mitigate the adverse effects of Ti and Nb on IGC resistance. First, optimizing the content of microalloying elements by carefully controlling the addition levels of Ti and Nb can help minimize the formation of coarse precipitates or detrimental inclusions at grain boundaries. Second, applying appropriate post-processing heat treatments, such as annealing, can promote a more homogeneous microstructure, refine the distribution of precipitates, and thereby reduce the susceptibility to localized corrosion.

5. Conclusion

The effect of microalloying elements Nb and Ti on the corrosion performance of Q&P-treated martensitic stainless steels was investigated by microstructure characterisation and electrochemical examination in two alloys, one containing Nb and Ti. The steels were processed under controlled laboratory conditions. The main conclusions were drawn as follows.

- Steels processed under laboratory conditions exhibited some microstructure differences compared to those produced industrially. The absence of MnS inclusions, the presence of segregation banding and, more interesting, the formation of Cr-carbides at the grain boundaries.
- Cr-carbide precipitates at grain boundaries, formed regardless of Nb and Ti addition, remained stable throughout the quenching and partitioning process.
- Microalloying elements Nb and Ti formed TiN(Nb) precipitates at GBs and grains, with a "core-shell" structure comprising early precipitation of TiN particles on which Nb precipitates.
- The electrochemical analysis showed that these microstructural differences lead to a preferential attack at grain boundaries (IGC) instead of localised pitting corrosion.
- In both alloys, the presence of Cr-carbides along GBs and Cr-depletion zones at the carbide-matrix interface region are the main reasons for IGC susceptibility when exposed to a corrosive environment.
- Alloy M showed higher IGC susceptibility than alloy B from the DOS analysis. The addition of Nb and Ti exacerbates the reactivity of the GBs due to the presence of additional particles, which are assumed to be cathodic with respect to the matrix.

These findings highlight a distinct corrosion mechanism in laboratory-processed Q&P steels, differing from the behaviour observed in industrially processed martensitic stainless steels. The influence of microalloying elements and precipitates on intergranular corrosion susceptibility was elucidated, offering new insights into the interplay between microstructure and localised corrosion in these advanced steels.

Declaration of competing interest

The authors declare that they have no known competing financial interests or personal relationships that could have appeared to influence the work reported in this paper.

Acknowledgement

This research has received funding from the European Unions Research Fund for Coal and Steel (RFCS) under grant agreement N°847195, QPINOX project.

References

[1] Fonstein N. Evolution of strength of automotive steels to meet customer challenges. Advanced high strength sheet steels. Cham: Springer; 2015. p. 1–16. https://doi.org/10.1007/978-3-319-19165-2.
[2] Wang W, Li M, He C, Wei X, Wang D, Du H. Experimental study on high strain rate behavior of high strength 600–1000 MPa dual phase steels and 1200 MPa fully martensitic steels. Mater Des 2013;47:510–21. https://doi.org/10.1016/j.matdes.2012.12.068.
[3] Grajcar A, Kuziak R, Zalecki W. Third generation of AHSS with increased fraction of retained austenite for the automotive industry. Arch Civ Mech Eng 2012;12(3):334–41. https://doi.org/10.1016/j.acme.2012.06.011.
[4] Contreras A, López A, Gutiérrez EJ, Fernández B, Salinas A, Deaquino R, et al. An approach for the design of multiphase advanced high-strength steels based on the behavior of CCT diagrams simulated from the intercritical temperature range. Mater Sci Eng, A 2020;772:138708. https://doi.org/10.1016/j.msea.2019.138708.
[5] Speer JG, Streicher AM, Matlock DK, Rizzo F, Krauss G. Quenching and partitioning: a fundamentally new process to create high strength trip sheet microstructures. Iron Steel Soc 2003:505–22.
[6] Speer JG, Matlock DK, De Cooman BC, Schroth JG. Carbon partitioning into austenite after martensite transformation. Acta Mater 2003;51:2611–22. https://doi.org/10.1016/S1359-6454(03)00059-4.
[7] Speer JG, Rizzo AssunçãoII FC, Matlock DK, Edmonds DV. The "quenching and partitioning" process: background and recent progress. Math Res 2005;8:417–23. https://doi.org/10.1590/S1516-14392005000400010.
[8] Tsuchiyama T, Tobata J, Tao T, Nakada N, Takaki S. Quenching and partitioning treatment of a low-carbon martensitic stainless steel. Mater Sci Eng, A 2012;532:585–92. https://doi.org/10.1016/j.msea.2011.10.125.
[9] Tobata J, Ngo-Huynh K, Nakada N, Tsuchiyama T, Takaki S. Role of silicon in quenching and partitioning treatment of low-carbon martensitic stainless steel. ISIJ Int 2012;52:1377–82. https://doi.org/10.2355/isijinternational.52.1377.
[10] Yuan L, Ponge D, Wittig J, Choi P, Jiménez JA, Raabe D. Nanoscale austenite reversion through partitioning, segregation and kinetic freezing: example of a ductile 2 GPa Fe–Cr–C steel. Acta Mater 2012;60:2790–804. https://doi.org/10.1016/j.actamat.2012.01.045.
[11] Huang Q, Schröder C, Biermann H, Volkova O, Mola J. Influence of martensite fraction on tensile properties of quenched and partitioned (Q&P) martensitic stainless steels. Steel Res Int 2016;87:1082–94. https://doi.org/10.1002/srin.201500472.
[12] Sierra-Soraluce A, Li G, Santofimia MJ, Molina-Aldareguia JM, Smith A, Muratori M, et al. Effect of microstructure on tensile properties of quenched and partitioned martensitic stainless steels. Mater Sci Eng, A 2023;864:144540. https://doi.org/10.1016/j.msea.2022.144540.
[13] Lu SY, Yao KF, Chen YB, Wang MH, Chen N, Ge XY. Effect of quenching and partitioning on the microstructure evolution and electrochemical properties of a martensitic stainless steel. Corros Sci 2016;103:95–104. https://doi.org/10.1016/j.corsci.2015.11.010.
[14] Kim JK, Kim YH, Uhm SH, Lee JS, Kim KY. Intergranular corrosion of Ti stabilized 11wt% Cr ferritic stainless steel for automotive exhaust systems. Corros Sci 2009;51:2716–23. https://doi.org/10.1016/j.corsci.2009.07.008.
[15] Kim JK, Lee BJ, Lee BH, Kim YH, Kim KY. Intergranular segregation of Cr in Ti-stabilized low-Cr ferritic stainless steel. Scripta Mater 2009;61:1133–6. https://doi.org/10.1016/j.scriptamat.2009.08.045.

[16] Kim JK, Kim YH, Kim KY. Influence of Cr, C and Ni on intergranular segregation and precipitation in Ti-stabilized stainless steels. Scripta Mater 2010;63:449–51. https://doi.org/10.1016/j.scriptamat.2010.05.002.
[17] Kim JK, Kim YH, Lee JS, Kim KY. Effect of chromium content on intergranular corrosion and precipitation of Ti-stabilized ferritic stainless steels. Corros Sci 2010; 52:1847–52. https://doi.org/10.1016/j.corsci.2010.01.037.
[18] Kim JK, Kim YH, Lee BH, Kim KY. New findings on intergranular corrosion mechanism of stabilized stainless steels. Electrochim Acta 2011;56:1701–10. https://doi.org/10.1016/j.electacta.2010.08.042.
[19] Kim JK, Lee JS, Kim KY. Intergranular precipitation and corrosion in weld of low Cr ferritic stainless steel. Met Mater Int 2012;18:619–24. https://doi.org/10.1007/s12540-012-4008-9.
[20] Park JH, Kim JK, Lee BH, Kim SS, Kim KY. Three-dimensional atom probe analysis of intergranular segregation and precipitation behavior in Ti–Nb-stabilized low-Cr ferritic stainless steel. Scripta Mater 2013;68:237–40. https://doi.org/10.1016/j.scriptamat.2012.10.022.
[21] Park JH, Kim JK, Lee BH, Seo HS, Kim KY. Effect of Zr addition on intergranular corrosion of low-chromium ferritic stainless steel. Scripta Mater 2014;76:77–80. https://doi.org/10.1016/j.scriptamat.2014.01.001.
[22] Park JH, Seo HS, Kim KY. Alloy design to prevent intergranular corrosion of low-Cr ferritic stainless steel with weak carbide formers. J Electrochem Soc 2015;162: C412–8. https://doi.org/10.1149/2.1001508jes.
[23] Li G, Li Z, Rahimi E, Muratori M, Smith A, Santofimia Navarro MJ, Gonzalez-Garcia Y. Pit initiation in quenching and partitioning processed martensitic stainless steels. Electrochim Acta 2024;498:144646. https://doi.org/10.1016/j.electacta.2024.144646.
[24] Li G, Kwakernaak C, Smith A, Muratori M, Gonzalez-Garcia Y, Santofimia MJ. Microstructure development of quenching and partitioning-processed martensitic stainless steels with different manganese content. Mater Sci Technol 2024;40: 449–65. https://doi.org/10.1177/02670836231215989.
[25] Taji I, Moayed MH, Mirjalili M. Orrelation between sensitisation and pitting corrosion of AISI 403 martensitic stainless steel. Corros Sci 2015;92:301–8. https://doi.org/10.1016/j.corsci.2014.12.009.
[26] Amadou T, Sidhom H, Braham C. Double loop electrochemical potentiokinetic reactivation test optimization in checking of duplex stainless steel intergranular corrosion susceptibility. Metall Mater Trans A 2004;35:3499–513. https://doi.org/10.1007/s11661-004-0187-4.
[27] Melitz W, Shen J, Kummel AC, Lee S. Kelvin probe force microscopy and its application. Surf Sci Rep 2011;66(1):1–27. https://doi.org/10.1016/j.surfrep.2010.10.001.
[28] Li G, Traka K, Kwarkernaak K, Gonzalez-Garcia Y, Santofimia MJ. Modelling the evolution of microstructural bands in a martensite/austenite Q&P-processed stainless steel. Scripta Mater 2025;257:116457. https://doi.org/10.1016/j.scriptamat.2024.116457.
[29] Hu S, Mao Y, Liu X, Han EH, Hänninen H. Intergranular corrosion behavior of low-chromium ferritic stainless steel without Cr-carbide precipitation after aging. Corros Sci 2020;166:108420. https://doi.org/10.1016/j.corsci.2019.108420.
[30] Charleux M, Poole WJ, Militzer M, Deschamps A. Precipitation behavior and its effect on strengthening of an HSLA-Nb/Ti steel. Metall Mater Trans A 2001;32: 1635–47. https://doi.org/10.1007/s11661-001-0142-6.
[31] Ma X, Miao C, Langelier B, Subramanian S. Suppression of strain-induced precipitation of NbC by epitaxial growth of NbC on pre-existing TiN in Nb-Ti microalloyed steel. Mater Des 2017;132:244–9. https://doi.org/10.1016/j.matdes.2017.07.006.
[32] Webel J, Mohrbacher H, Detemple E, Britz D, Mücklich F. Quantitative analysis of mixed niobium-titanium carbonitride solubility in HSLA steels based on atom probe tomography and electrical resistivity measurements. J Mater Res Technol 2022;18:2048–63. https://doi.org/10.1016/j.jmrt.2022.03.098.
[33] Zeng Z, Li C, Li Z, Zhai Y, Wang J, Li Z. Effect of Nb content and thermal deformation on the microstructure and mechanical properties of high-strength anti-seismic rebar. Mater Sci Eng, A 2022;840:142929. https://doi.org/10.1016/j.msea.2022.142929.
[34] Chen H, Lu L, Huang Y, Li X. Insight into TiN inclusion induced pit corrosion of interstitial free steel exposed to aerated NaCl solution. J Mater Res Technol 2021; 13:13–24. https://doi.org/10.1016/j.jmrt.2021.04.046.
[35] Ralston KD, Birbilis N. Effect of grain size on corrosion: a review. Corrosion 2010; 66. https://doi.org/10.5006/1.3462912. 075005–075005-13.